



HAL
open science

Enriched kinematic fields of cracked structures

Carole Henninger, Stéphane Roux, François Hild

► **To cite this version:**

Carole Henninger, Stéphane Roux, François Hild. Enriched kinematic fields of cracked structures. *International Journal of Solids and Structures*, 2010, 47 (24), pp.3305-3316. 10.1016/j.ijsolstr.2010.08.012 . hal-00535952

HAL Id: hal-00535952

<https://hal.science/hal-00535952>

Submitted on 14 Nov 2010

HAL is a multi-disciplinary open access archive for the deposit and dissemination of scientific research documents, whether they are published or not. The documents may come from teaching and research institutions in France or abroad, or from public or private research centers.

L'archive ouverte pluridisciplinaire **HAL**, est destinée au dépôt et à la diffusion de documents scientifiques de niveau recherche, publiés ou non, émanant des établissements d'enseignement et de recherche français ou étrangers, des laboratoires publics ou privés.

Enriched kinematic fields of cracked structures

Carole Henninger, Stéphane Roux, François Hild

*Laboratoire de Mécanique et Technologie (LMT-Cachan)
ENS Cachan/CNRS-UMR 8535/Université Paris 6/PRES UniverSud Paris
61 avenue du Président Wilson
F-94235 Cachan Cedex, France*

Abstract

Far from the crack tip process zone where non-linear phenomena take place, the mechanical behavior of a cracked medium can be analyzed within the framework of elasticity. Apart from the classical singular stress field associated with the elastic behavior, the effect of a confined process zone is decomposed over a set of (super-singular) fields. Because these fields are indexed by the exponent of their decay with distance from the crack tip, the dominant effect of non-linear mechanisms is characterized by the amplitudes of the first super-singular fields (modes I and II). This approach provides a macroscopic characterization of crack tip non-linearities and describes accurately the displacement field. As an application, the cyclic loading of a cracked elasto-plastic medium is discussed.

Keywords:

Williams' series, displacement field, global approach to fracture

Email address: `carole.henninger,stephane.roux,francois.hild@lmt.ens-cachan.fr`
(Carole Henninger, Stéphane Roux, François Hild)

1. Introduction

Linear elastic fracture mechanics has proven to capture the most salient features of fracture, even though it is based on a seemingly elastic description of the solid. The reason for this success is the fact that the elastic singular crack field relies on the mechanical behavior outside the confined crack tip zone where non-linear processes (e.g. damage in composites [1, 2] and concrete [3], plasticity in metals [4, 5, 6]) take place. As such, it allows the far-field (possibly complicated) elastic loading to be linked with the local crack tip through few meaningful loading parameters, for instance, stress intensity factors [7].

However, this reduction to (three-mode) characteristic loading may appear for some applications to be too crude to allow for a meaningful analysis. This is the case in fatigue for an elasto-plastic material, where at the level of the stress intensity factors, no change is expected past the first loading cycle. These problems call for an extended or enriched characterization, which is the motivation of the present work. In the following analysis, more emphasis is put on the kinematics of the problem. The reason for this is the development of measurement techniques yielding accurate estimates of full-field displacements [8]. Among them, digital image correlation was used to address different aspects related to the presence of cracks in a solid. For instance, stress intensity factors [9, 10, 11], crack tip opening angles [12] or crack opening displacements [13] and toughness [14] are measured with a low uncertainty levels.

To address the question of enrichment, let us follow the basic philosophy underlying linear elastic fracture mechanics, namely, outside the confined process zone where dissipative mechanisms are active, the mechanical behavior of many solids remains linear elastic. Moreover, it is through this elastic field that the crack tip interacts

with the external load applied to the solid. Thus the approach will be based on a characterization of the elastic field radiating from the crack tip. In that sense, it departs from the analysis recently proposed by Ma *et al.* [15], in which the process zone is the main focus. Similarly, the Modified Boundary Layer (MBL) method [16], which consists in matching the boundary conditions with the singular field dictated by the stress intensity factor and the next non-singular field (T-stress), allows for the study of non-linearities *within* the process zone. In contrast, the aim of the present work is to propose an enrichment of such boundary conditions that can be seen as a signature in the elastic domain of the confined non-linearities of the process zone. Conversely, it is in the same spirit as that proposed by Pommier and Hamam [17] even though the kinematic bases are different.

To solve the problem, one cuts out of the studied domain a zone \mathcal{D} containing the crack tip process zone, and one substitutes to it an equivalent boundary condition on $\partial\mathcal{D}$. The elastic field outside \mathcal{D} is identical to the elasto-plastic solution of the medium with its complete geometry. At this stage, the applied loading on $\partial\mathcal{D}$ is unknown. Moreover, as in linear elastic fracture mechanics [18], it is assumed that the medium is infinite, and devoid of any loading (this hypothesis will be revisited in the sequel). At this level of generality, the elastic problem for an *arbitrary* loading is solved. Such a task is easily performed within the framework of plane elasticity by resorting to complex potentials [19, 20, 7].

All elastic fields that fulfill the crack face boundary conditions (*i.e.*, the traction on this boundary vanishes) are easily obtained [20]. Moreover, they are naturally *ranked*. A basis for such space of elastic fields is constructed from functions that have a power law dependence with the distance r to the crack tip, with an exponent α_n for the n th field. Sorting out these functions with respect to exponent α_n allows one to rank them according to their far-field influence. This structure is similar to

a multipole expansion encountered for instance in electrostatics [21]. Among those fields, the usual mode I and mode II displacement fields [19, 7] are found. Looking for an enriched description, it suffices to browse this library of functions and keep only the lowest orders, at a level that will be judged satisfactory. This point will be addressed later on.

The result of this analysis is that a description of the crack kinematics is completed from the usual stress intensity factors (SIF) description, by a few additional parameters that are the dominant corrections in the elastic field due to the non-linearity occurring in the process zone. In the case of cyclic loading where a small amount of plastic flow at the crack tip is taking place at each cycle, it will be shown that even for a periodic SIF evolution, those additional “enriched” parameters may follow a non-periodic change, leading to fatigue. The paper is organized as follows. First, the elastic solution is derived in plane elasticity, and the basis of functions alluded to above is identified. A physical interpretation of those fields is given. The ability of a reduced set of fields to offer an accurate description of the displacement field is then illustrated on an elasto-plastic case solved by using a finite element approach. The cyclic loading is characterized with the additional terms of the description and interpreted in the framework of perfect plasticity.

2. Elastic fields

2.1. Displacement eigenfunctions

Within the framework of plane elasticity, the solution to an elastic problem is reduced to the identification of two analytic functions of the complex variable $z = x + iy$, $\varphi(z)$ and $\psi(z)$, the so-called Kolosov-Muskhelishvili potentials [19]. From

the latter, the displacement field $U = U_x + iU_y$ reads

$$2\mu U \equiv \kappa\varphi(z) - z\overline{\varphi}'(z) - \overline{\psi}(z) \quad (1)$$

where μ is the shear modulus and κ a dimensionless (Kolossof) material constant related to Poisson's ratio, ν , through $\kappa = (3-4\nu)$ for plane strain or $\kappa = (3-\nu)/(1+\nu)$ for plane stress conditions.

The crack tip is here assumed to be at the origin of the coordinate system ($z = 0$) and the crack lies along the negative real axis (see Fig. 1a).

$$z = x + iy = re^{i\theta}$$

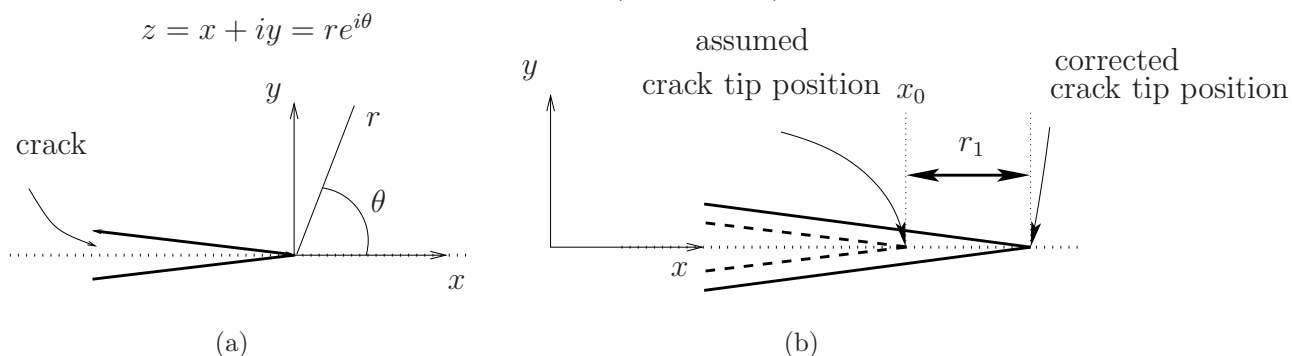


Figure 1: (a) Sketch of the crack and coordinate systems used in the theoretical development; (b) Representation of crack tip offset r_1 . The origin of the coordinate system is shifted.

Thus the traction $t = \sigma_{yy} + i\sigma_{yx}$, along the crack faces is expressed as [19]

$$t = \varphi'(z) + \overline{\varphi}'(z) + \overline{z}\varphi''(z) + \psi'(z) , z = re^{\pm i\pi} \quad (2)$$

No characteristic scale is involved in the considered formulation. Consequently, φ and ψ are homogeneous functions of z , *i.e.*, proportional to z^α .

The crack face boundary condition, $t = 0$, implies that a non-trivial solution is obtained for potentials of the form $\varphi(z) = Az^{n/2}$ and $\psi(z) = Bz^{n/2}$, where n is an integer, and for the following relation between potential amplitudes

$$B = -(n/2)A - (-1)^n \overline{A} \quad (3)$$

In order to define more precisely the various contributions, let us write the displacement along the crack faces

$$2\mu U(r, \theta = \pm\pi) = r^{n/2} e^{\pm i\pi n/2} (\kappa + 1) A \quad (4)$$

A first distinction arises from the consideration of displacement continuity across the crack, namely, odd exponents ($n = 1 - 2m$) involve a discontinuity whereas even exponents $n = -2m$ correspond to continuous displacement fields.

It can also be noticed that the displacement on each crack face is aligned with the A direction, which allows one to associate two modes with each exponent n , namely, $\Re A$ and $\Im A$. In particular, for odd exponents, real values of A correspond to displacements along the y direction, whereas purely imaginary values of A correspond to displacements along the x direction.

Thus the displacement fields Ω_n (resp. Υ_n) corresponding to any exponent n and $A = 1/\sqrt{2\pi}$ (resp. $A = i/\sqrt{2\pi}$) read

$$\Omega_n = \frac{1}{2\mu\sqrt{2\pi}} r^{n/2} [\kappa e^{in\theta/2} - (n/2)e^{i(2-n/2)\theta} + ((-1)^n + n/2)e^{-in\theta/2}] \quad (5)$$

$$\Upsilon_n = \frac{i}{2\mu\sqrt{2\pi}} r^{n/2} [\kappa e^{in\theta/2} + (n/2)e^{i(2-n/2)\theta} + ((-1)^n - n/2)e^{-in\theta/2}] \quad (6)$$

so that the most general field is written as

$$U = \sum_n [\omega_n \Omega_n(z) + v_n \Upsilon_n(z)] \quad (7)$$

where ω_n and v_n are real numbers, with dimension $\text{MPa}\cdot\text{m}^{1-n/2}$.

The factor $\sqrt{2\pi}$ is introduced here to match the standard singular crack field definition [7], obtained for $n = 1$. The stress intensity factors K_I and K_{II} thus correspond precisely to the amplitudes ω_1 and v_1 of Ω_1 , and Υ_1 respectively. In pure

mode I, the crack opening discontinuity reads

$$\begin{aligned}
[[U]] &\equiv i(U_y^+ - U_y^-) \\
&= i \sum_n \omega_n \left(\Im(\Omega_n)(r, \theta = +\pi) - \Im(\Omega_n)(r, \theta = -\pi) \right) \\
&= i \frac{\kappa + 1}{\mu\sqrt{2\pi}} \sum_{n \text{ odd}} (-1)^{(1-n)/2} \omega_n r^{n/2}
\end{aligned} \tag{8}$$

and in pure mode II

$$\begin{aligned}
[[U]] &\equiv (U_x^+ - U_x^-) \\
&= \sum_n v_n \left(\Re(\Upsilon_n)(r, \theta = +\pi) - \Re(\Upsilon_n)(r, \theta = -\pi) \right) \\
&= -\frac{\kappa + 1}{\mu\sqrt{2\pi}} \sum_{n \text{ odd}} (-1)^{(1-n)/2} v_n r^{n/2}
\end{aligned} \tag{9}$$

For $n = 2$ the classical T-stress contribution [20] and the rigid body rotation are retrieved from Ω_n and Υ_n respectively.

The fields that are more singular than the usual crack solution are referred to as “supersingular” (*i.e.*, $n < 0$), and those that are less, are termed “subsingular” (*i.e.*, $n > 1$).

The subsingular fields have no impact on the crack tip kinematics. However, since the corresponding stress fields increase with the distance to the crack tip, they are useful to match the singular fields with the remote geometry and the boundary conditions. This use will be exemplified in the sequel with a numerical example in which the crack has a finite extent.

On the contrary, the stress fields associated with supersingular fields are dominant at the process zone scale so that they carry the most important information in the analysis of a fracture process, as will be argued in the sequel. Note that these supersingular fields are usually ignored because their asymptotic behavior near the crack tip leads to an unbounded energy density [18]. In the present linear elastic

analysis, the crack tip process zone is excluded because of its non-linear behavior (see Section 3.1), thus there is no need to reject these solutions.

The first supersingular mode I field Ω_{-1} is seen as the superposition of two usual mode I crack fields with crack tips located at $-\delta/2$ and $+\delta/2$, and with SIFs equal to $-K$ and $+K$ respectively, in the limit where δ tends to 0, and K diverges, while the product $K\delta$ remains finite. This field is thus interpreted as a *dipole* of cracks. Similarly the second odd supersingular mode I field, Ω_{-3} , is a quadrupole, and generally the supersingular fields form a *multipole hierarchy*. Mode II fields obey the same structure.

In the following section, this structure is exploited to yield characteristic features of the crack tip process zone.

2.2. Interpretation of supersingular fields

Noting that consecutive order functions are related through

$$\frac{\partial \Omega_n}{\partial x} = \frac{n}{2} \Omega_{n-2} \quad \text{and} \quad \frac{\partial \Upsilon_n}{\partial x} = \frac{n}{2} \Upsilon_{n-2} \quad (10)$$

a simple recurrence thus provides

$$\frac{\partial^n \Omega_1}{\partial x^n} = \frac{(-1)^{n+1} (2n)!}{(2n-1)2^{2n} n!} \Omega_{1-2n} \quad (11)$$

for $n \geq 1$. The same expression also holds for the mode II functions.

To highlight the role of ω_{-1} , the crack tip is now assumed to be located at $z = z_0 = (x_0, 0)$ (Fig. 1b). If one uses expansion (7) together with the derivation

property (11), one notes that

$$\begin{aligned}
\omega_1\Omega_1(z - z_0) + \omega_{-1}\Omega_{-1}(z - z_0) &= \omega_1\left(\Omega_1(z - z_0) + 2\frac{\omega_{-1}}{\omega_1}\frac{\partial\Omega_1(z-z_0)}{\partial x}\right) \\
&= \omega_1\left(\Omega_1(z - z_0) - 2\frac{\omega_{-1}}{\omega_1}\frac{\partial\Omega_1(z-z_0)}{\partial x_0}\right) \\
&= \omega_1\left(\Omega_1(z - z_0) + r_1\frac{\partial\Omega_1(z-z_0)}{\partial x_0}\right) \text{ with } r_1 = -2\frac{\omega_{-1}}{\omega_1} \\
&= \omega_1\Omega_1(z - (z_0 + r_1))
\end{aligned} \tag{12}$$

where $\frac{\partial}{\partial x_0} = -\frac{\partial}{\partial x}$ is the derivative with respect to the crack tip position on the x -axis, x_0 .

This expression is a first order Taylor expansion of a usual crack field whose tip would be located at position $z_0 + r_1$ (Fig. 1b), where

$$r_1 = -2\frac{\omega_{-1}}{\omega_1} \tag{13}$$

Since the crack tip vicinity is affected by non-linear mechanisms (in the process zone), the exact position of the tip is ambiguous, but it has to be defined to allow for reliable measurements of crack advance, for instance. For the present analysis, the most relevant choice is the one that allows for the best match with the far elastic field. As shown in Equation (12), an offset in the crack tip position generates essentially an ω_{-1} correction to the K_I -field. The crack tip position is therefore *defined* such that $\omega_{-1} = 0$. Once this position is prescribed, the first non-trivial correction is a quadrupolar term

$$\omega_1\Omega_1 + \omega_{-3}\Omega_{-3} = \omega_1\left[\Omega_1 - 4\frac{\omega_{-3}}{\omega_1}\frac{\partial^2\Omega_1}{\partial x^2}\right] \tag{14}$$

that is independent of the crack tip location and hence intrinsic to the process zone. Additional corrections decay more quickly to infinity with r than Ω_{-3} . Hence it is the dominant enrichment to linear elastic fracture mechanics. Dimensionally the ratio $8\omega_{-3}/\omega_1 \equiv r_2^2$ is interpreted as proportional to the square of the extent of the process zone, r_2 .

2.3. Summary of the approach

With the above results, the analysis of non-linear fracture kinematic fields is addressed. First, the core of the process zone has to be defined and omitted from any subsequent analysis. The outside displacement field is then decomposed over the basis of functions Ω_n (mode I) and Υ_n (mode II). The effective crack tip position is estimated from the relative importance of the ω_{-1} and ω_1 (or v_{-1} and v_1) amplitudes. Moving the crack tip so that the $n = -1$ amplitude vanishes, allows for the characterization of a process zone size from the $n = -3$ field amplitude.

3. Application to a test case

The studied material has an elastic-plastic behavior with Young's modulus $E = 200$ GPa, Poisson's ratio $\nu = 0.30$, and an initial yield stress $\sigma_y = 400$ MPa. It follows a J2-flow rule. A plastic behavior close to perfect plasticity is chosen in order to interpret the results with a simple model (see Section 5). For this reason and in order to avoid numerical problems, a very small hardening (yield stress 450 MPa for 100% plastic strain) is prescribed. The hardening is chosen linear isotropic for the sake of computation rapidity and it can be assumed that the results would be identical if a kinematic hardening was chosen, since the loading is never compressive (see below). Let us stress that in this example the process zone is identified with the plastic region at the crack tip. However, the proposed formalism is equally applicable to other types of non-linear behaviors.

The analyzed geometry is a square sample of edge length $2b = 2$ m. A centered crack is present, its length ($2a = 20$ mm) corresponds to 1% of the plate width so that an infinite medium is a legitimate approximation. Geometrical and loading symmetries allow for the modeling of only a quarter of the plate with the appropriate

boundary conditions $U_x = 0$ on the left-hand edge and $U_y = 0$ on the non-cracked part of the bottom edge (Fig. 2). The crack edges and the right-hand edge are traction-free.

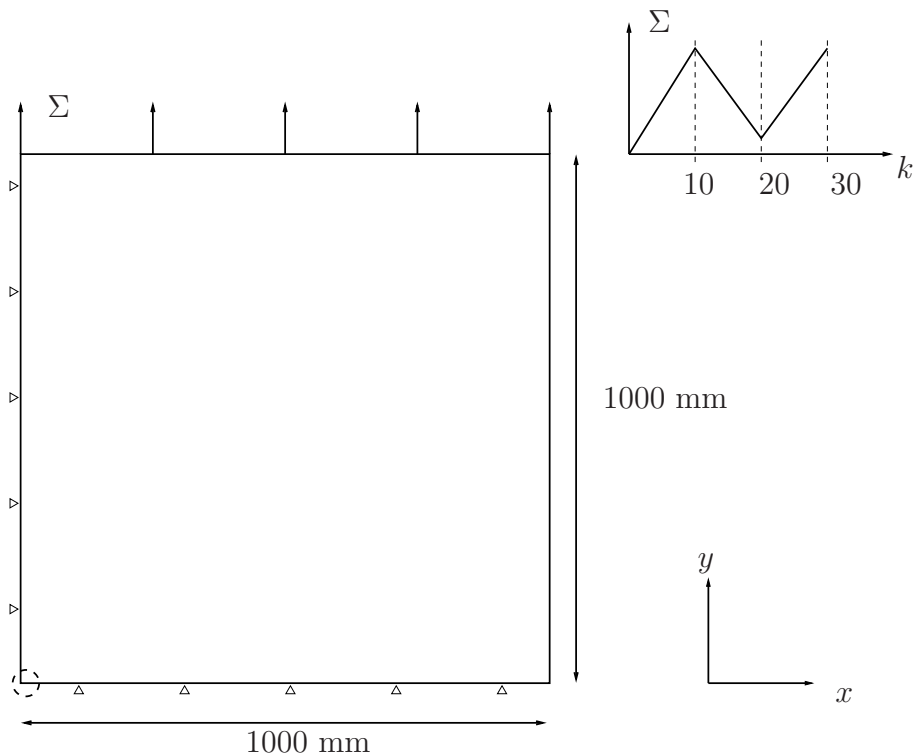


Figure 2: Dimensions, load and boundary conditions of the model (quarter of real sample). The half-crack is located at the bottom left edge, along the x direction.

To investigate the ability of the description to account for a plastic behavior in the process zone, a tensile load-unload-reload sequence is simulated, namely, the sample is subjected to a variable uniaxial remote tension Σ applied in three phases. First a loading part where the stress on the edge of the square is progressively increased to 200 MPa in ten steps. In a second stage, the stress is decreased down to 20 MPa, again in ten steps. Last, in a third stage, the stress is increased up to 200 MPa in

ten steps. Thus 30 different steps have been carried out and the displacement field of each of these states has been recorded.

The finite element computations are performed with ABAQUS [22] on a free triangular mesh of 48421 CPE3 elements (plane strain assumption and linear interpolation) and 24545 nodes (Fig. 3). The mesh is refined in the crack tip vicinity so that the edge of the first element near the crack tip is approximately $5 \mu\text{m}$ (Fig. 3c).

3.1. Displacement projection

The displacement field in the elastic domain is projected onto the previously introduced basis. Because of the symmetry of the problem, only mode I fields are considered. Supersingular fields are considered down to the order $n = N_0 = -3$ (*i.e.*, quadrupolar crack field). Subsingular functions are necessary to account for the fact that the crack has a finite extent. A maximum order of $N_1 = 8$ was selected. As shown in Fig. 4, the stress intensity factor at maximum loading is quite stable within the range $[-5; -3]$ for N_0 , and for $N_1 \geq 8$, and the discrepancy with the theoretical value of the SIF (see Equation (18)) remains below 2% for the chosen truncation ($N_0 = -3$; $N_1 = 8$) (see also Fig. 11b).

Hence, the displacement reads

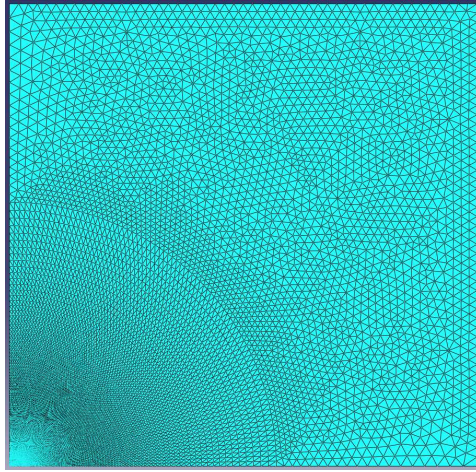
$$U_{fit}(x, y) = \sum_{n=-3}^8 \omega_n \Omega_n(z - z_0) \quad (15)$$

where z_0 is the crack tip position. The projection is performed on a zone bounded by R_{in} and R_{out} , which are chosen relatively to the dominance of the K_I field and the expected information given by supersingular modes. The outer radius R_{out} is arbitrarily chosen to be 28 mm and complementary studies not discussed herein show that outer radii taken in the range 15 – 50 mm do not affect the meaningful amplitudes (SIF and supersingular amplitudes) by more than 5%. The cut-off radius

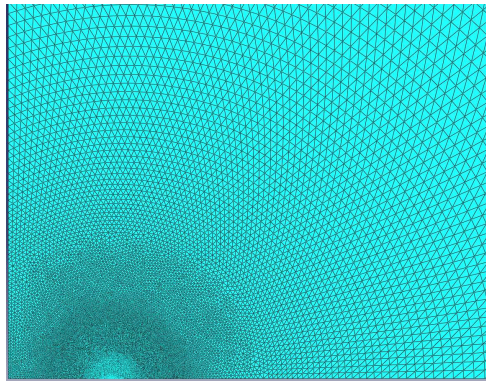
R_{in} is introduced because the displacement field cannot be described with the basis of elastic fields at the crack tip where confined plasticity occurs. This radius takes the value 0.2 mm. It is approximately the level of the plastic radius ρ in plane strain (estimated with von Mises' criterion) at maximum loading

$$\rho = \frac{K_I^2}{2\pi\sigma_y^2}(1 - 2\nu)^2 \quad (16)$$

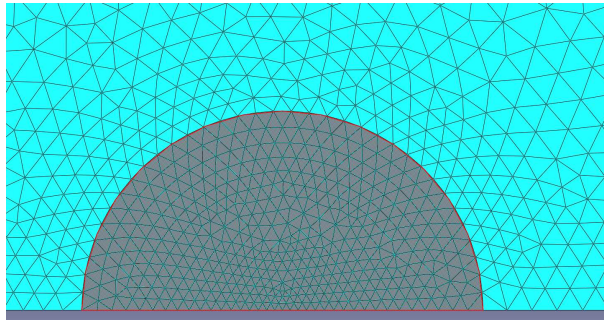
At this distance from the crack tip, the K_I field is the most dominant mode after the translation ($n = 0$), as shown in Fig. 5a and c. The next most important contributions are those from the supersingular fields, and as expected, such contributions far from the crack tip (Fig. 5b and d) are very weak. Besides, their non-proportional change along the loading history (Fig. 5c and d) proves that they are affected by crack tip plasticity, as highlighted by the comparison with the elastic case (Fig. 5e and f). This will be further commented in Section 4. On the contrary, all subsingular amplitudes follow the loading history - the bump for mode $n = 4$ (Fig. 5c and d) is an artifact of the logarithmic scale due to a sign reversal of ω_4 .



(a) Mesh of the whole model ($1 \times 1 \text{ m}^2$)



(b) View of a zone of size $40 \times 40 \text{ mm}^2$



(c) Zoom on crack tip zone (radius 0.2 mm)

Figure 3: Mesh of the numerical case. One quarter is modeled (a). Detail of the mesh for the whole crack (b) and zoom around the crack tip (c).

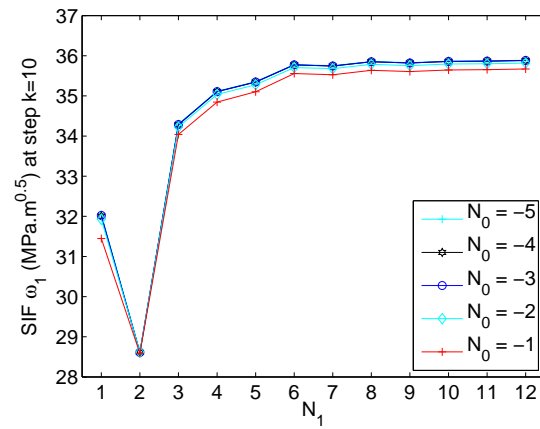
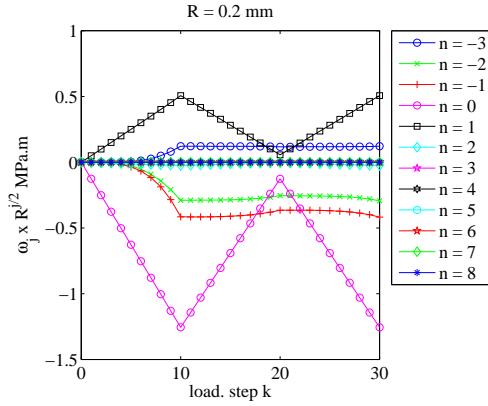
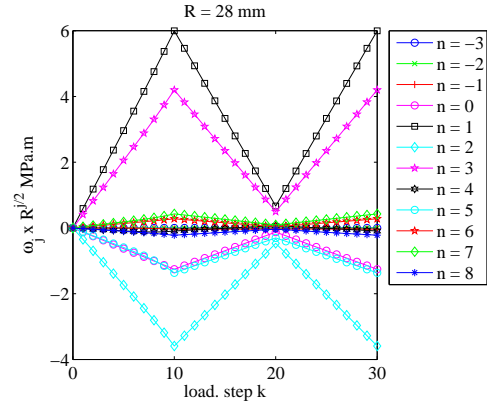


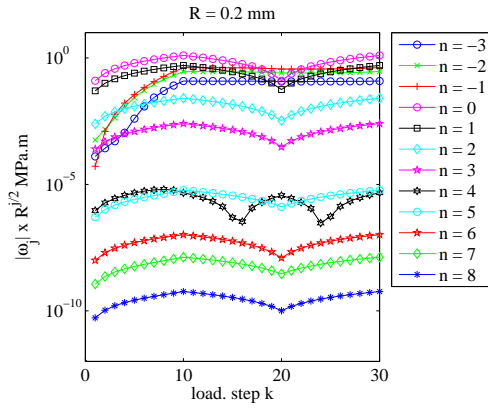
Figure 4: Stress intensity factor at maximum loading ($k = 10$) vs. maximum order N_1 in Williams' decomposition, for various minimum orders N_0 .



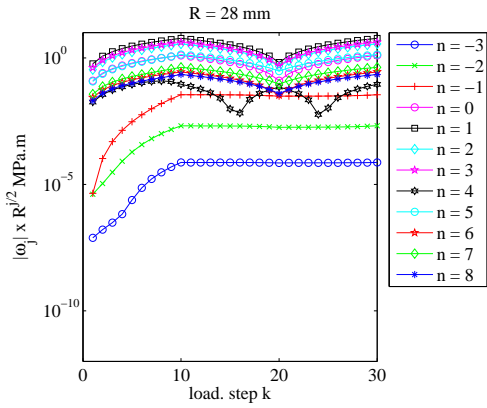
(a) $R = R_{in}$



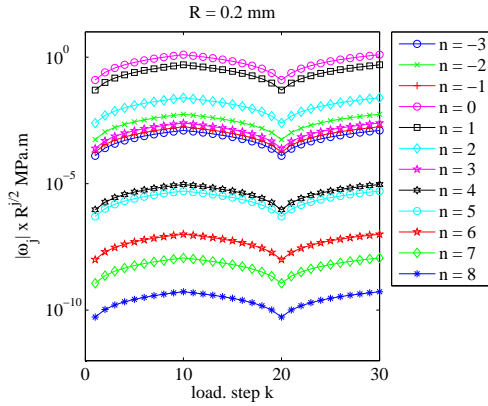
(b) $R = R_{out}$



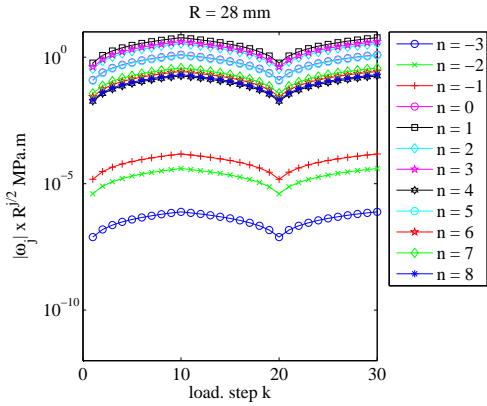
(c) $R = R_{in}$ - Logarithmic scale



(d) $R = R_{out}$ - Logarithmic scale



(e) $R = R_{in}$ - Log. scale - Elastic



(f) $R = R_{out}$ - Log. scale - Elastic

Figure 5: Influence of each mode from $n = -3$ to $n = 8$ at $R = R_{in} = 0.2$ mm (a-c-e) and $R = R_{out} = 28$ mm (b-d-f) in linear (a-b) and logarithmic (c-d, e-f) scales. Figures a, b, c and d correspond to the elasto-plastic model, and figures e and f refer to the elastic case.

3.2. Validity of the description at various stages of loading

A quality estimate based on the displacement residual is defined as

$$\varepsilon = \frac{\langle \|U_{\text{FEM}} - U_{\text{fit}}\| \rangle}{\sigma(U_{\text{FEM}})} \quad (17)$$

where U_{FEM} denotes the computed displacement field (it may also be the measured one when experimental data are used), U_{fit} corresponds to the mode I decomposition (15), and σ the root mean square value of U_{FEM} . The denominator is chosen to make the error estimator dimensionless. Let us also note that this quality estimate is based on a uniform measure over all nodes of the finite element computation, and not a weight proportional to the element area. Because of the mesh refinement close to the crack tip, this quality measure is strongly weighted by the crack tip. Moreover, other error measures could have been chosen. In particular, measures with a mechanical content are an alternative (*e.g.*, based on constitutive equation gap [23, 24, 25]). They are not considered since the identification procedure developed herein aims at using full field displacement measurements. The latter information is the raw data to be processed. Fig. 6 shows that the residual error remains always less than 6×10^{-3} so that the global quality of the analysis is deemed satisfactory. The highest level of error is reached at maximum unloading ($k = 20$), when the discrepancy between the plastic displacement U_{FEM} and the elasticity-based projection U_{fit} is maximum. For the maximum load ($k = 10$ or $k = 30$), error $\varepsilon \leq 10^{-3}$ and hence, the process zone influence is well captured by this approach.

From the finite element simulation, the field of cumulative plastic strain is determined. The latter is comparable for the maximum load levels ($k = 10$ or $k = 30$). Fig. 7 shows the equivalent strain field for $k = 30$. The plastic strain is confined to a rather small neighborhood of the crack tip. A disk of radius 0.5 mm cuts out most of the plastic strain. In the present analysis, a smaller disk was chosen (*i.e.*,

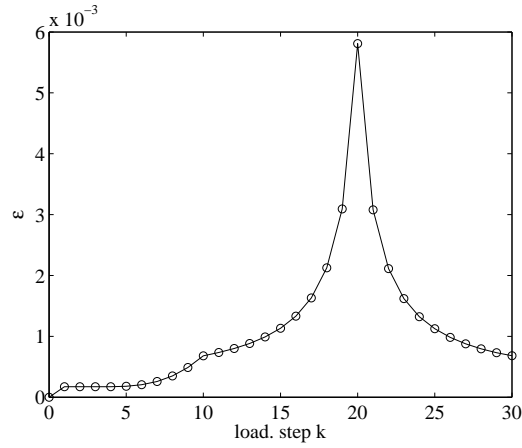


Figure 6: Dimensionless residual error change for the entire loading history. The error peaks at maximum unloading ($k = 20$), but still remains below 6×10^{-3} .

$R_{in} = 0.2$ mm), which still leaves in the analyzed domain some significant plastic deformation.

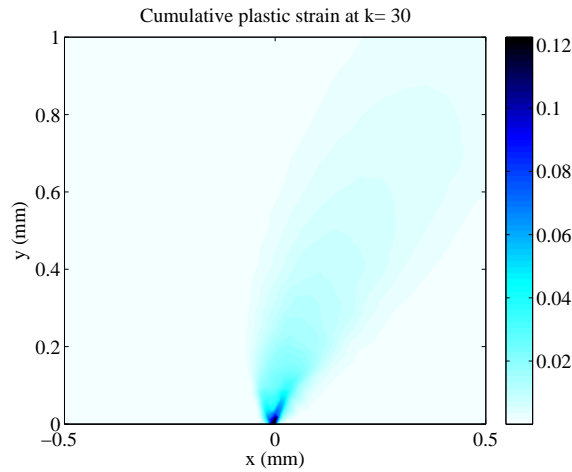


Figure 7: Map of equivalent cumulative plastic strain at the end of the reloading cycle ($k = 30$).

A detailed comparison of the displacement components U_x and U_y are shown in

Fig. 8 and 9, respectively. On the left, finite element results are shown, and on the right the fit of the data with 12 fields. Moreover each figure presents a wide map ($20 \times 20 \text{ mm}^2$), and two close-up views in the vicinity of the crack tip ($4 \times 2 \text{ mm}^2$ and $1 \times 1 \text{ mm}^2$). The difference between FEM and fitted displacement components in the close neighborhood of the crack tip is plotted in Fig. 10. The maximum relative errors for both components are located near the crack tip (where plastic deformation takes place) and are approximately equal to 30%. Yet, purely elastic fields still fit the displacement data very accurately.

The amplitude ω_1 corresponds to the mode I stress intensity factor. Its change along the loading history is shown in Fig. 11a and compared (Fig. 11b) to the tabulated values K_I^{th} resulting from an LEFM assumption [26]

$$K_I^{th} = \Sigma \sqrt{\pi a} (1.0 + 0.128a/b - 0.288(a/b)^2 + 1.523(a/b)^3) \quad (18)$$

Fig. 11b also shows the relative error of the SIF estimated from the J -integral

$$K_I = \sqrt{\frac{EJ}{1-\nu^2}} \quad (19)$$

with respect to the tabulated values K_I^{th} . The J -integral is computed with ABAQUS on a quadrangular mesh, on a domain containing the crack tip and spreading over a distance of approximately 1.3 mm from it.

The amplitude ω_1 follows strictly the change of the stress on the edge of the sample and deviates very slightly from the reference value, as if the material were purely elastic. The ratio of K_I over the applied stress Σ is not constant, but varies only slightly in the range $[0.176, 0.200]$ along the entire loading history. Furthermore, the tangent SIF, $dK_I/d\Sigma$, remains almost constant, with a maximum deviation of 6.2% as compared with its first value (Fig. 12).

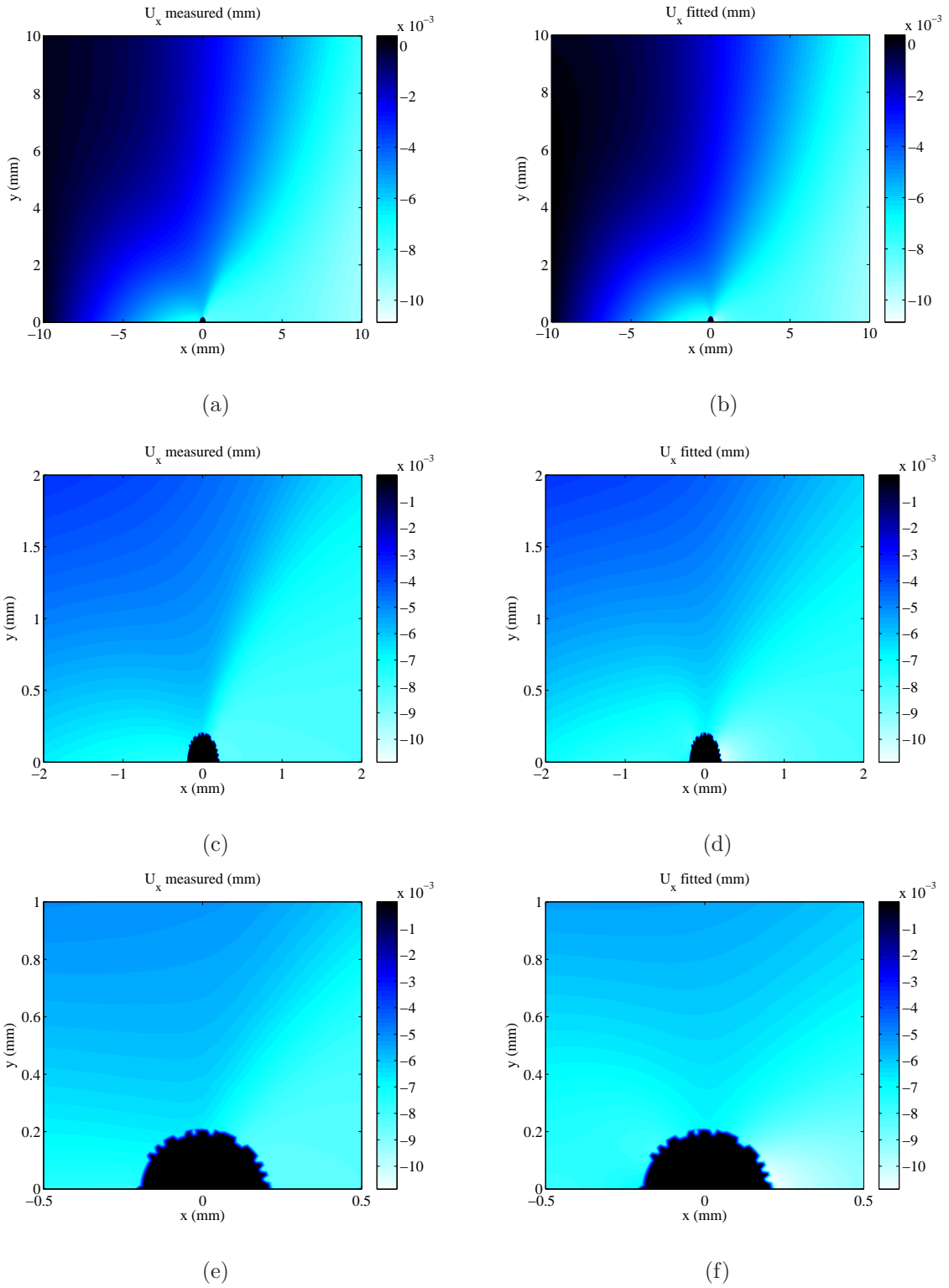


Figure 8: Comparison between U_x obtained as FEM results (left figures a, c and e) or fitted (right figures b, d and f), over a 20×20 mm² square (top a and b), close-up views of a 4×2 mm² rectangle (middle c and d) and a 1×1 mm² square (bottom e and f) at the end of the entire loading history $k = 30$.

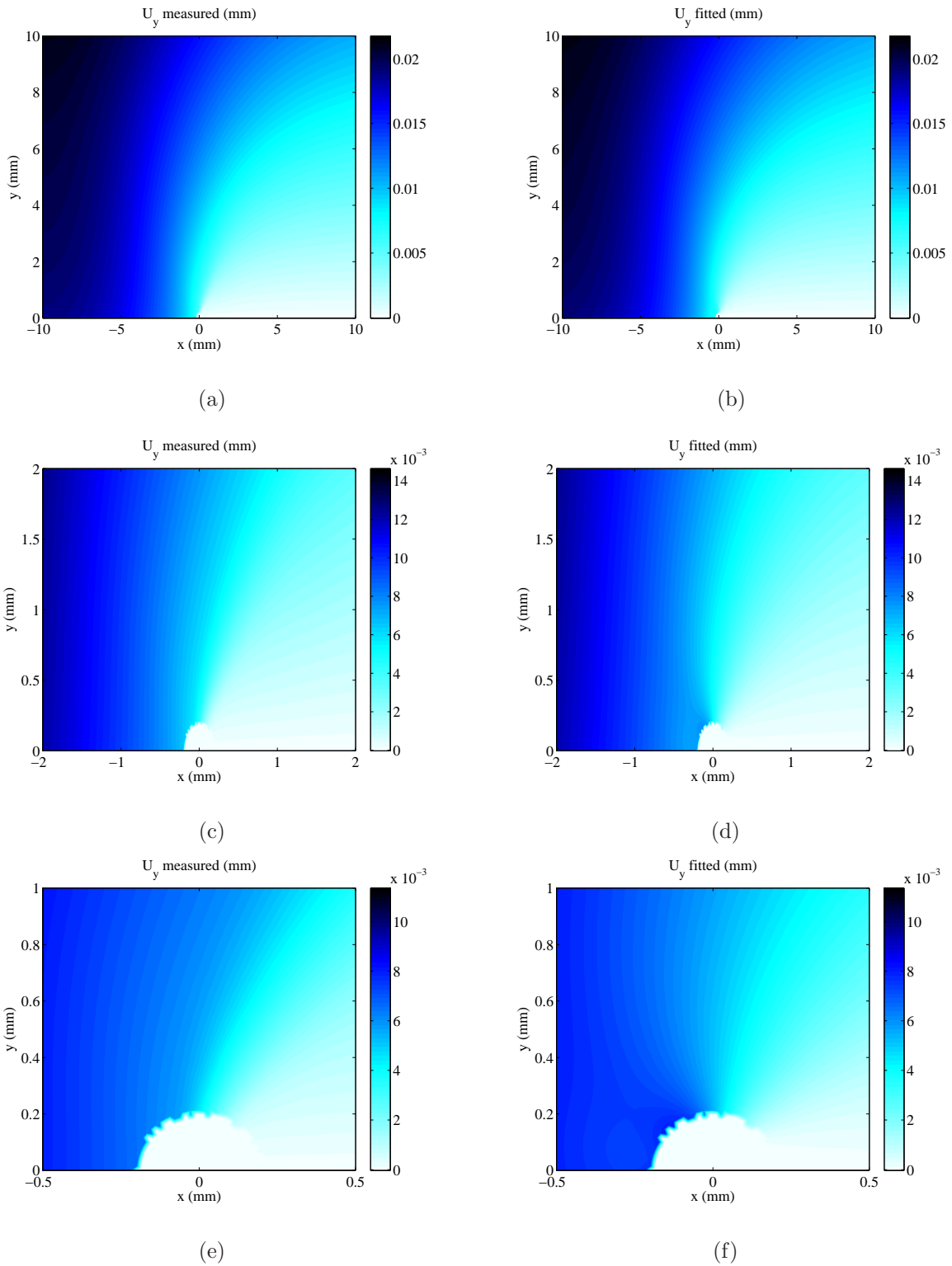


Figure 9: Comparison between U_y obtained as FEM results (left figures a, c and e) or fitted (right figures b, d and f), over a 20×20 mm² square (top a and b), close-up views of a 4×2 mm² rectangle (middle c and d) and a 1×1 mm² square (bottom e and f) at the end of the entire loading history $k = 30$.

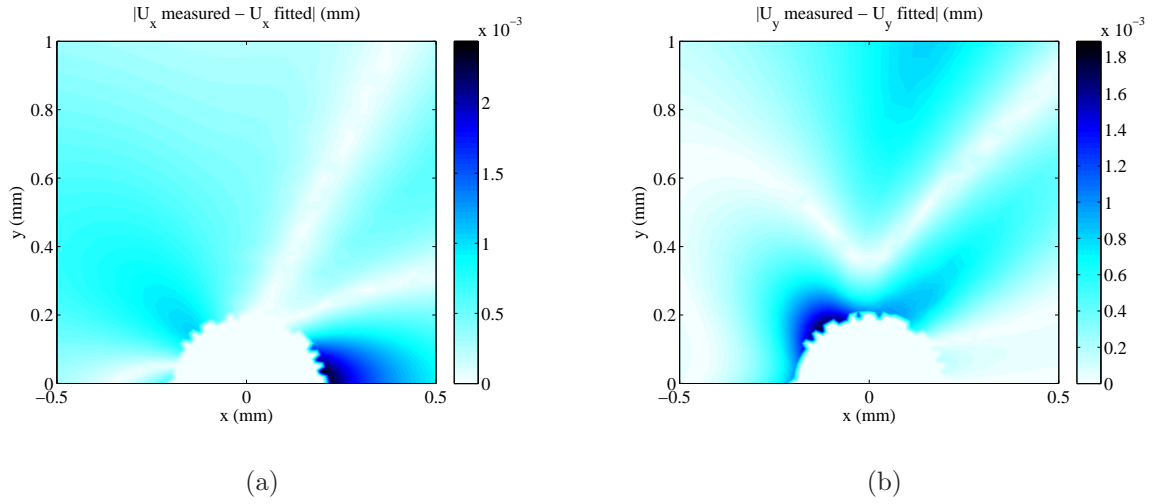


Figure 10: Difference between measured and fitted U_x (a) and U_y (b) over a 1×1 mm² square at the end of the entire loading history $k = 30$. The maximum relative errors with respect to the FE computation are approximately 30% for both components.

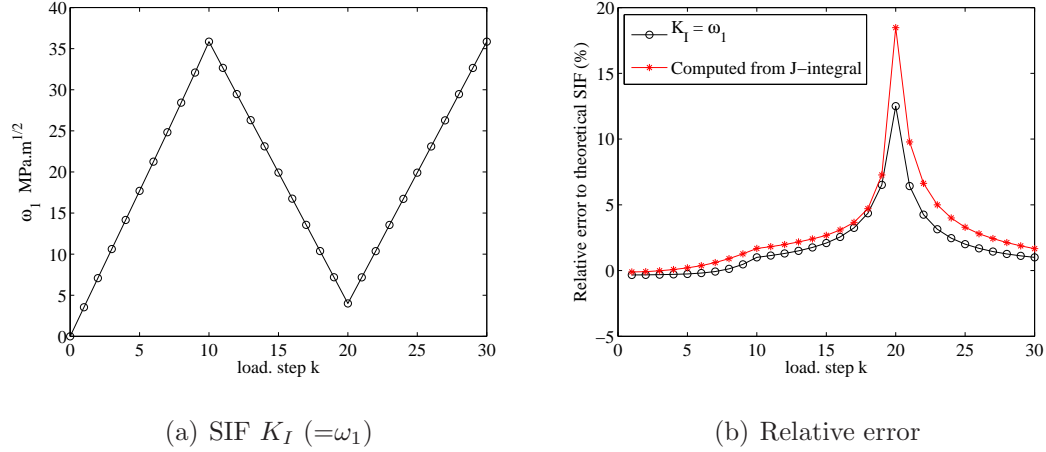


Figure 11: Change of the SIF $K_I = \omega_1$ as a function of loading step k (a) and error relative to the tabulated value of K_I (b). The relative error is compared to that of the SIF estimated from the J -integral computed with ABAQUS.

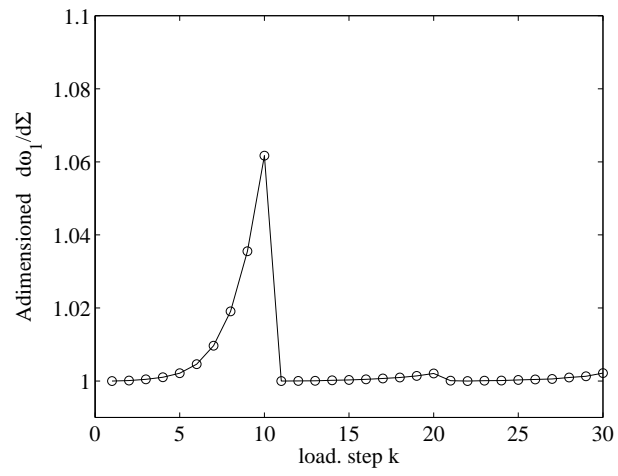


Figure 12: Tangent SIF (normalized by its value at $k = 1$) vs. loading step k .

4. Cyclic loading: Macroscopic characterization

The identification of the entire sequence of 30 loading steps is now commented. As earlier mentioned, subsingular and supersingular fields have to be distinguished. Subsingular fields essentially reflect the loading history. Since the associated stress increases with the distance to the crack tip, the amplitude of these fields is mainly dictated by the far-field boundary conditions, and hence they do follow the loading history (Fig. 5).

Fig. 13 shows the amplitudes of the two odd supersingular contributions along the loading history. The fact that these two plots do not follow the mere loading stress signals that they are influenced by the effect of plasticity at the crack tip (see also Fig. 5).

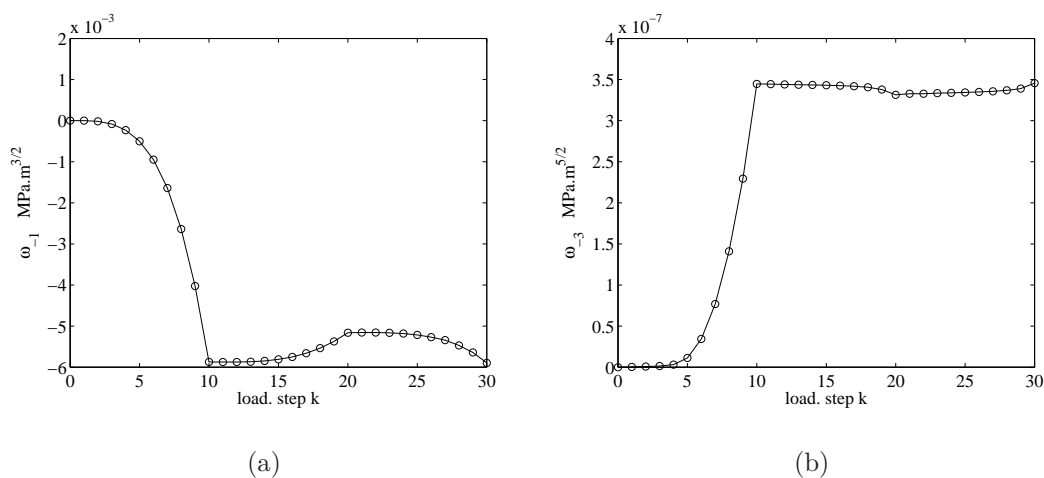


Figure 13: Supersingular amplitudes ω_{-1} (a) and ω_{-3} (b) vs. loading step k .

Rather than ω_{-1} and ω_{-3} , it was shown above that these amplitudes allow for the definition of a crack tip offset r_1 , and a process zone width r_2 . The former is computed from Equation (13) at the first projection (see Equation (15)) and shown in Fig. 14a.

The process zone width r_2 is defined once the crack tip has been moved. Fig. 14b shows several computations of r_2 versus loading step, corresponding to successive projections aiming at canceling out ω_{-1} . At iteration $(k + 1)$, the projection of the displacement field (see Equation (15)) is achieved with the corrected crack tip position $z_0 + r_1$, where r_1 is computed with Equation (13) at iteration (k) . The process zone width change is close to that from the first identification, except for the values around the maximum unloading $k = 20$.

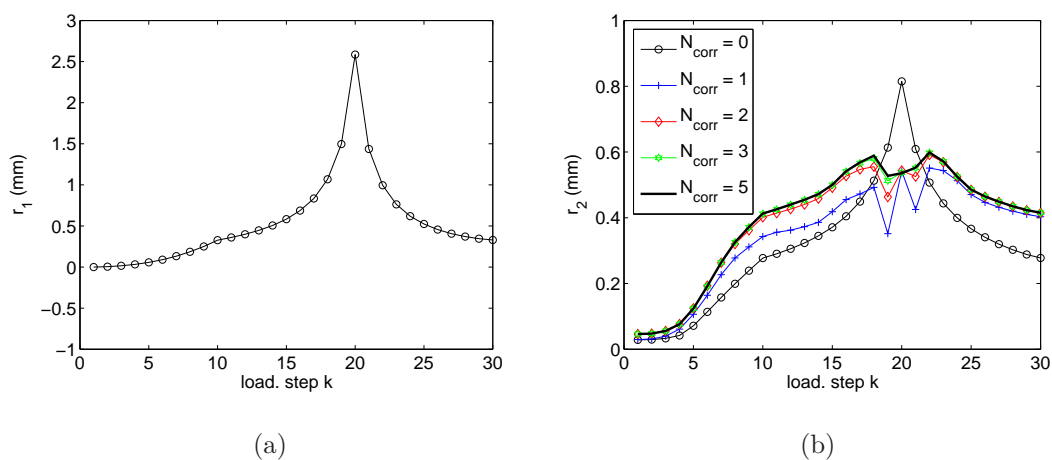


Figure 14: Change with loading step k of (a) the crack tip offset, (b) the process zone width at first projection ($N_{corr} = 0$) and after successive corrections of crack tip location ($N_{corr} > 0$).

It is interesting to relate either the supersingular amplitudes or the corresponding length scales as functions of the SIF ω_1 , as shown respectively in Fig. 15 and 16. In the former, the supersingular amplitudes ω_{-1} and ω_{-3} follow a dependence with ω_1 reminiscent of a quasi-ideal elasto-plastic behavior. The formation of the plastic zone during the first loading stage is characterized by a strong increase in the supersingular amplitudes. During unloading, these amplitudes remain almost constant, and virtually reversible, so that the state reached for $k = 30$ is very close

to the end of the first loading period ($k = 10$).

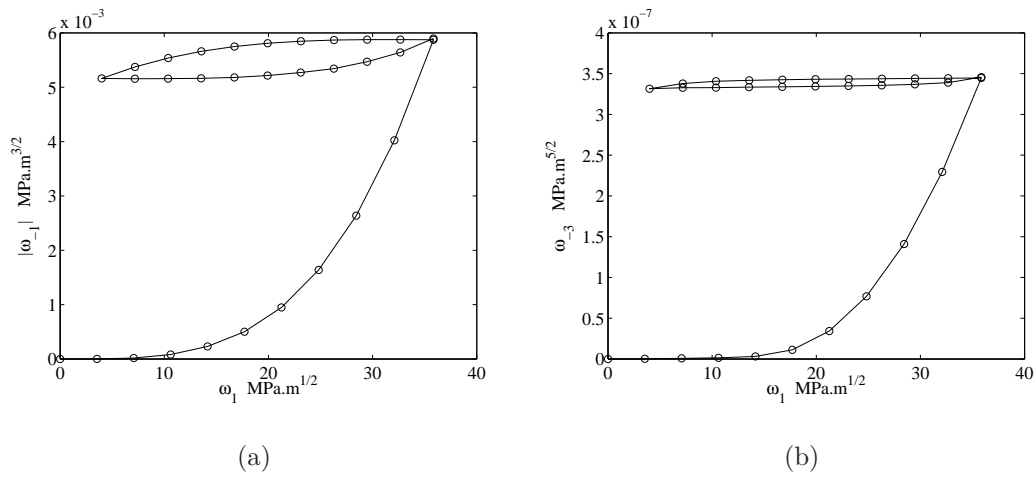


Figure 15: Supersingular amplitudes $|\omega_{-1}|$ (a) and ω_{-3} (b) vs. SIF ω_1 .

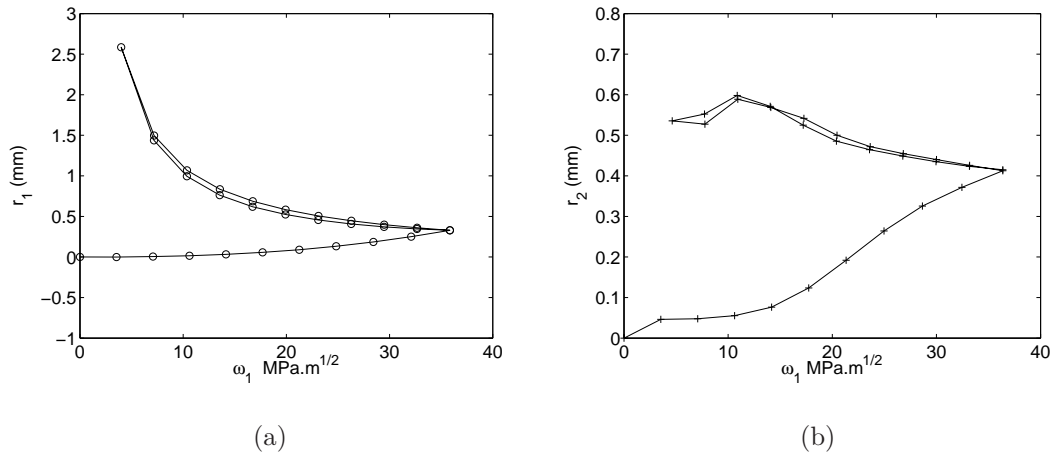


Figure 16: Crack tip offset r_1 (a) and process zone size r_2 (b) (after correction of crack tip location) vs. SIF ω_1 .

5. Cyclic loading: Interpretation

An interesting observation leading to a simplified picture of the mechanics at play is to consider the tangent SIF, $dK_I/d\Sigma$, where the finite difference between loading steps is considered instead of the derivative. In Fig. 12, this quantity is further normalized to its first value, where plasticity is essentially negligible. It is observed that at load reversal the incremental behavior is essentially elastic. However as loading or unloading proceed, a small but significant deviation from unity is observed. Thus plasticity takes place upon unloading and the small hysteresis observed, *e.g.*, in Fig. 15, during unloading and reloading is not an identification artifact.

In this section, a simple interpretation of the previous observations is proposed. To proceed, the problem is simplified and an elastic-perfectly plastic behavior is assumed (the absence of hardening is a simplification as compared to the chosen constitutive law for the previous simulation, even though the hardening modulus was very small as compared to the Young's modulus).

5.1. Loading

Let us assume that the problem has been solved for a given stress level Σ^{ref} . Outside the plastic process zone, the elastic field is assumed to be characterized by amplitudes ω_n^{ref} for fields Ω_n . From the latter, it is easy to deduce the solution to the problem for an arbitrary level Σ of a monotonic loading. The SIF, or ω_1 , is proportional to the load level. However, what will dictate the extension of the process zone is the yield stress. Since no other scale is specified, the plastic radius is used to rescale all distances, and match the reference case. From this argument, the plastic radius scales as

$$\rho_p \sim \frac{(\omega_1^{ref})^2 \Sigma^2}{(\Sigma^{ref})^2 \sigma_y^2} \quad (20)$$

All amplitudes are further related

$$\omega_n \propto \sigma_y \rho_p^{1-n/2} \propto \sigma_y \left(\frac{\omega_1}{\sigma_y} \right)^{2-n} \quad (21)$$

Thus amplitudes ω_n are linked with ω_1 through

$$\omega_n \propto \omega_1^{2-n} \quad (22)$$

The crack tip offset $r_1 = -2\omega_{-1}/\omega_1$ is thus expected to scale as

$$r_1 \propto \omega_1^2 \propto \rho_p \quad (23)$$

The next supersingular amplitude, ω_{-3} , scales as

$$\omega_{-3} \propto \omega_1^5 \quad (24)$$

so that the size of the process zone r_2 also scales as r_1 or ρ_p . Fig. 17 probes the proportionality of $\omega_{-1}^{1/3}$ and $\omega_{-3}^{1/5}$ with ω_1 . A linear behavior is observed, especially for the first supersingular amplitude.

5.2. Unloading

At the end of the loading stage, a developed plastic zone has been created where von Mises' stress has reached the yield stress. Upon unloading, it is expected that, incrementally, the usual singular crack field is to be subtracted to the stress state. However, this would produce a diverging stress at the crack tip that will induce reverse plastic flow. Thus the incremental displacement field is rather the one observed during the loading stage, but since one started with a stress field that was the yield limit, the effective yield stress that is seen is in fact twice as large [27]. The previous results are used to relate the decrease of amplitude $\Delta\omega_n$ versus the decrease of stress intensity factor

$$\Delta\omega_n \propto 2\sigma_y \left(\frac{\Delta\omega_1}{2\sigma_y} \right)^{2-n} \quad (25)$$

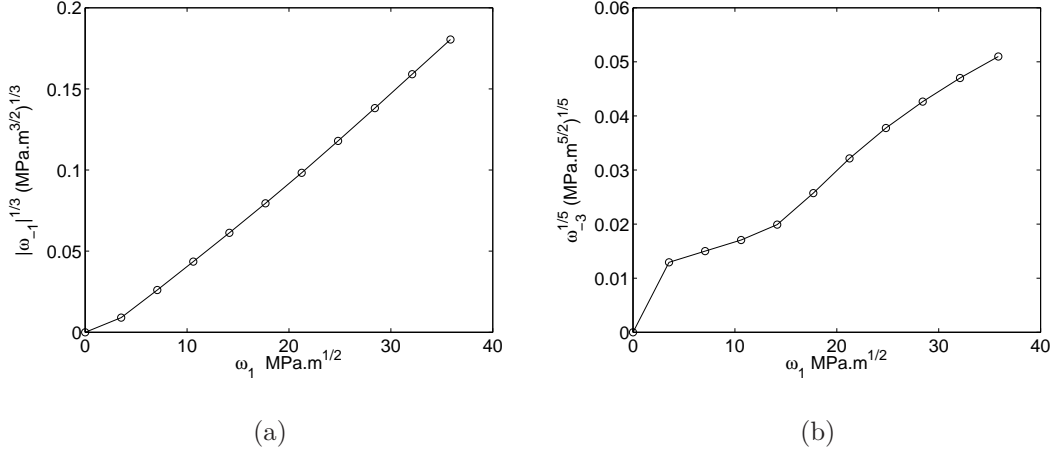


Figure 17: Supersingular amplitudes $|\omega_{-1}|$ (a) and ω_{-3} (b) raised to the expected power (resp. 1/3 and 1/5) vs. SIF, for the first loading stage.

To avoid the dependence of the above quantity with the yield stress, let us introduce the supersingular amplitudes at the maximum load, with a superscript *

$$\frac{\Delta\omega_n}{\omega_n^*} = 2^{n-1} \left(\frac{\Delta\omega_1}{\omega_1^*} \right)^{2-n} \quad (26)$$

This result predicts a simple universal unloading characteristics, close to Masing's rule [28] in plasticity.

5.3. Reloading

During the reloading stage, the same incremental law is used (provided no other intermediate radius reaches the yield stress). Fig. 18 shows a comparison between the observed normalized amplitudes ω_{-1} and ω_{-3} and the proposed model. Some differences are observed, but still the main features are captured.

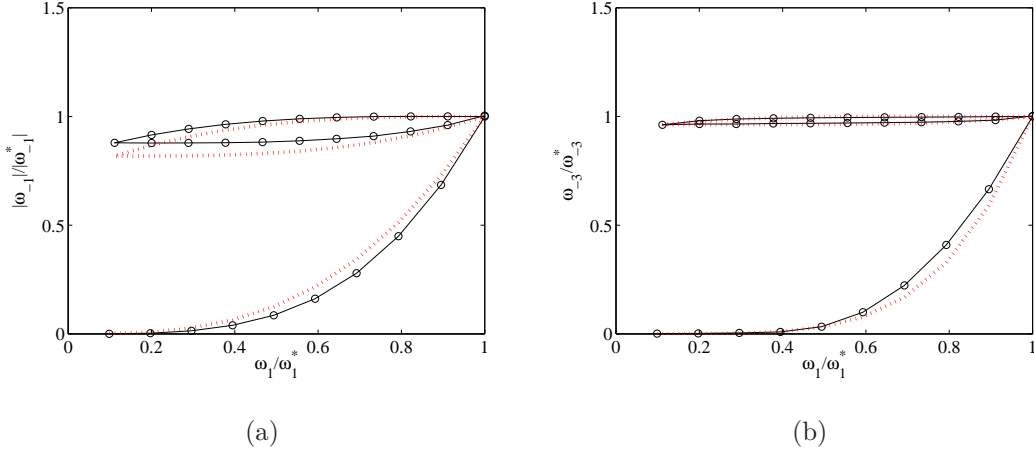


Figure 18: Scaled supersingular amplitudes ω_{-1} (a) and ω_{-3} (b) vs. normalized SIF (open circle and solid line) as compared to the simple model shown as a dotted line.

6. Conclusion

The crack kinematics was analyzed in terms of an enriched set of "multipolar" crack modes consisting in classical modes I and II fields, as well as subsingular and supersingular fields. The latter accounts for the effect of non-linear mechanisms close to the crack tip on the elastic components when the core of the process zone is not considered. The definition of a suited library of displacement fields is a key ingredient to a reliable evaluation of the crack geometry (*e.g.*, crack tip location). This procedure is especially of interest when experiments are analyzed and the crack tip location is unknown.

The approach proposed herein was compared with finite element simulations for a material with an elasto-plastic behavior. When applied to a loading-unloading-reloading cycle, it is shown that supersingular amplitudes are needed to describe the crack kinematics. In particular, a simplified analysis is able to capture the salient trends associated with a cyclic load history. The methodology used in this paper is

directly applicable to a broad class of different materials (brittle to ductile) and test geometries for which the process zone is small as compared to the region of interest.

This type of analysis may also be used in experiments. Two routes can be followed. First, an a posteriori analysis of the measured displacement field similar to the one carried out herein, where the measured field is used instead of the computed one. Another one, referred to as an integrated analysis [11], considers the library of displacement fields Ω_n and Υ_n and performing, for instance, digital image correlation to identify directly the unknown components ω_n and v_n . It corresponds to yet another way of using the concept of “diffuse stress gauging” [29, 30]. By using an integrated approach, the support of the gauge is diffuse on the sample face. In that sense, it is a “crack gauge” that measures, for instance, stress intensity factors, but also crack tip location and a first characterization of confined non-linearity.

It is of interest to extend the present analysis to more complex loading conditions to address, for instance, mixed mode crack loading, or the initial stage of fatigue where plastic yielding is more developed. Investigating three dimensional fatigue cracks using X-ray tomography constitutes also a very challenging direction for future investigation [31, 32].

Acknowledgments

This work was funded by the French National Agency for Research (ANR) through the project RUPXCUBE (ANR-09-BLAN-0009-01 grant): “ Three-dimensional identification of local crack propagation laws with X-ray tomography, full-field measurements and extended finite element simulations.”

- [1] S. M. Spearing and A. G. Evans, The role of fiber bridging in the delamination resistance of fiber-reinforced composites, *Acta Metall. Mater.* **40** [9] (1992) 2191-2199.

- [2] B. Budiansky, J. W. Hutchinson and A. G. Evans, Matrix fracture in fiber-reinforced ceramics, *J. Mech. Phys. Solids* **34** [2] (1986) 167-189.
- [3] Z. P. Bažant, Size effect in blunt fracture: concrete, rock, metal, *J. Engrg Mech. ASCE* **110** (1984) 518-535.
- [4] J. W. Hutchinson, Singular behavior at the end of a tensile crack in a hardening material, *J. Mech. Phys. Solids* **16** (1968) 18-31.
- [5] J. W. Hutchinson, Plastic stress and strain fields at a crack tip, *J. Mech. Phys. Solids* **16** (1968) 337-347.
- [6] J. R. Rice and G. F. Rosengren, Plane strain deformation near a crack tip in a power-law hardening material, *J. Mech. Phys. Solids* **16** (1968) 1-12.
- [7] G. R. Irwin, Analysis of the stresses and strains near the end of a crack traversing a plate, *ASME J. Appl. Mech.* **24** (1957) 361-364.
- [8] P. K. Rastogi, eds., Photomechanics, (Springer, Berlin (Germany), 2000), **77**.
- [9] S. R. McNeill, W. H. Peters and M. A. Sutton, Estimation of stress intensity factor by digital image correlation, *Eng. Fract. Mech.* **28** [1] (1987) 101-112.
- [10] J. Réthoré, A. Gravouil, F. Morestin and A. Combescure, Estimation of mixed-mode stress intensity factors using digital image correlation and an interaction integral, *Int. J. Fract.* **132** (2005) 65-79.
- [11] F. Hild and S. Roux, Measuring stress intensity factors with a camera: Integrated Digital Image Correlation (I-DIC), *C.R. Mécanique* **334** (2006) 8-12.
- [12] D. S. Dawicke and M. S. Sutton, CTOA and crack-tunneling measurements in thin sheet 2024-T3 aluminum alloy, *Exp. Mech.* **34** (1994) 357-368.

- [13] M. A. Sutton, W. Zhao, S. R. McNeill, J. D. Helm, R. S. Piascik and W. T. Ridel, Local crack closure measurements: Development of a measurement system using computer vision and a far-field microscope, in: *Advances in fatigue crack closure measurement and analysis: second volume, STP 1343*, R. C. McClung and J. Newman, J.C., eds., (ASTM, 1999), 145-156.
- [14] P. Forquin, L. Rota, Y. Charles and F. Hild, A method to determine the toughness scatter of brittle materials, *Int. J. Fract.* **125** [1] (2004) 171-187.
- [15] F. Ma, M. A. Sutton and X. Deng, Plane strain mixed mode crack-tip stress fields characterized by a triaxial stress parameter and a plastic deformation extent based characteristic length, *J. Mech. Phys. Solids* **49** (2001) 2921-2953.
- [16] Z.-Z. Du and J. W. Hancock, The effect of non-singular stresses on crack-tip constraint, *J. Mech. Phys. Solids* **39** [4] (1991) 555-567.
- [17] S. Pommier and R. Hamam, Incremental model for fatigue crack growth based on a displacement partitioning hypothesis of mode I elastic-plastic displacement fields, *Fat. Fract. Engrg. Mater. Struct.* **30** [7] (2007) 582-598.
- [18] M. F. Kanninen and C. H. Popelar, *Advanced fracture mechanics*, (Oxford University Press, 1985).
- [19] N. I. Muskhelishvili, *Some basic problems of the mathematical theory of elasticity*, (P. Noordholl Ltd, Groningen (Holland), 1953).
- [20] M. L. Williams, On the stress distribution at the base of a stationary crack, *ASME J. Appl. Mech.* **24** (1957) 109-114.

- [21] R. E. Raab and O. L. de Lange, Multipole theory in electromagnetism: classical, quantum, and symmetry aspects, with applications, (Oxford University Press, 2004).
- [22] http://www.simulia.com/products/abaqus_standard.html
- [23] P. Ladevèze, *Comparaison de modèles de milieux continus*, (thèse d'Etat, Université Paris 6, 1975).
- [24] R. V. Kohn and B. D. Lowe, A variational method for parameter identification, *Math. Mod. Num. Ana.* **22** [1] (1988) 119-158.
- [25] G. Geymonat, F. Hild and S. Pagano, Identification of elastic parameters by displacement field measurement, *C. R. Mécanique* **330** (2002) 403-408.
- [26] G. C. Sih, Handbook of stress-intensity factors: Stress-intensity factor solutions and formulas for reference, Bethlehem, Pa (USA), Lehigh University (1973), 815 p.
- [27] J. R. Rice, Mechanics of crack tip deformation and extension by fatigue, *Proceedings Fatigue crack propagation, STP 415*, (ASTM, Philadelphia (USA), 1967), 247-309.
- [28] G. Masing, Eigenspannungen und Vertfestigung beim Messing, *Proceedings of the Second International Congress of Applied Mechanics, Zurich, Switzerland* (1926) 332â5 [in German].
- [29] S. Roux, F. Hild and S. Pagano, A stress scale in full-field identification procedures: a diffuse stress gauge, *Eur. J. Mech. A/Solids* **24** (2005) 442-451.

- [30] F. Hild and S. Roux, Digital image correlation: from measurement to identification of elastic properties - A review, *Strain* **42** (2006) 69-80.
- [31] N. Limodin, J. Réthoré, J.-Y. Buffière, A. Gravouil, F. Hild and S. Roux, Crack closure and stress intensity factor measurements in nodular graphite cast iron using three-dimensional correlation of laboratory X-ray microtomography images, *Acta Mater.* **57** [14] (2009) 4090-4101.
- [32] N. Limodin, J. Réthoré, J.-Y. Buffière, F. Hild, S. Roux, W. Ludwig, J. Rannou and A. Gravouil, Influence of closure on the propagation of fatigue cracks in a nodular cast iron investigated by X-ray tomography and 3D Volume Correlation, *Acta Mater.* **58** [8] (2010) 2957-2967.